RALDH1 Inhibition Shows Immunotherapeutic Efficacy in Hepatocellular Carcinoma

Pengfei Yu[1,2], Shuwen Cao[1], Shyh-Ming Yang[3], Ganesha Rai[3], Natalia J. Martinez[3], Adam Yasgar[3], Alexey V. Zakharov[3], Anton Simeonov[3], William A. Molina Arocho[1], Graham P. Lobel[1,4], Hesham Mohei[1], Alexis L. Scott[1], Li Zhai[1], Emma E. Furth[1], M. Celeste Simon[4,5], and Malay Haldar[1,4,6]

ABSTRACT

Globally, hepatocellular carcinoma (HCC) is one of the most commonly diagnosed cancers and a leading cause of cancer-related death. We previously identified an immune evasion pathway whereby tumor cells produce retinoic acid (RA) to promote differentiation of intratumoral monocytes into protumor macrophages. Retinaldehyde dehydrogenase 1 (RALDH1), RALDH2, and RALDH3 are the three isozymes that catalyze RA biosynthesis. In this study, we have identified RALDH1 as the key driver of RA production in HCC and demonstrated the efficacy of RALDH1-selective inhibitors (Raldh1-INH) in suppressing RA production by HCC cells. Raldh1-INH restrained tumor growth in multiple mouse models of HCC by reducing the number and tumor-supporting functions of intratumoral macrophages as well as increasing T-cell infiltration and activation within tumors. Raldh1-INH also displayed favorable pharmacokinetic, pharmacodynamic, and toxicity profiles in mice thereby establishing them as promising new drug candidates for HCC immunotherapy.

Introduction

Hepatocellular carcinoma (HCC) is a devastating disease with a projected annual incidence of around one million cases worldwide by 2025 (1). Around 27,000 people die from this disease each year in the United States alone and advanced HCC has an abysmal 5-year survival rate of about 2% (2, 3). Surgical resection and liver transplantation are preferred treatments for early-stage HCC, whereas locoregional interventions such as radiofrequency ablation and transarterial chemoembolization are used in unresectable cases (3). Advanced metastatic cases present substantial management challenges with a median survival of a few months. Recent progress in systemic therapies, which currently include immune checkpoint blockers (ICB), tyrosine kinase inhibitors, and angiogenesis inhibitors, has improved patient outcomes. Nonetheless, there is substantial room for improvement, especially with immunotherapy. Single-agent ICB elicits clinical responses in a minority of patients, suggesting the existence of other biological modulators of ICB responses (4).

Macrophages and dendritic cells (DC) are the key antigen-presenting cells in solid tumors and, given the current limitations of immunotherapy, there has been increasing interest in therapeutically targeting them (5). These efforts are generally aimed at reducing the frequency of immunosuppressive macrophages, increasing the frequency of tumoricidal and pro-inflammatory macrophages, and enhancing the immunostimulatory activities of DCs (5). A number of approaches have been described previously that can achieve these effects in experimental models by targeting specific receptors and/or pathways in tumor-associated macrophage (TAM) and DCs (6, 7). In contrast, we know very little about whether and how we can target monocyte differentiation into DCs versus TAMs for cancer immunotherapy. DCs and TAMs can also originate from nonmonocyte precursors—embryonic progenitors arising from yolk sac and HSC-derived myeloid progenitors, respectively—but these progenitors are exceeding rare compared with abundant circulating monocytes (8, 9). Furthermore, DCs and TAMs within the tumor microenvironment (TME) have a finite lifespan requiring a continuous influx of progenitors (10). Thus, targeting monocyte differentiation represents a viable but largely unexplored therapeutic strategy in cancer immunotherapy.

We previously discovered that some tumors produce retinoic acid (RA) that promotes differentiation of monocytes into immunosuppressive and tumor-promoting macrophages (11). Therefore, reducing RA production by tumor cells or inhibiting RA signaling in monocytes is a potential treatment approach in these tumors. Key barriers to implementation of this approach include identifying the tumors where this pathway is active and developing safe and effective inhibitors of the RA pathway. Here, we report that HCCs produce high levels of RA through overexpression of retinaldehyde dehydrogenase 1 (RALDH1), which is one of the three enzymes that catalyzes RA production (12). RA production in HCC was abrogated by RALDH1 inhibitors (Raldh1-INH) we recently developed (13). These inhibitors suppressed tumor growth in multiple mouse models of human and murine HCC. Using genetic and pharmacologic tools, we demonstrate that the HCC-suppressive effects of Raldh1-INH are driven by altered macrophage numbers and function as well as increased infiltration of tumors by activated T cells. Pharmacological and toxicological analyses revealed a favorable profile of Raldh1-INH for potential clinical use, which was also supported by observations in newly generated RALDH1 knockout (RALDH1-KO) mice. These findings provide proof of concept for the use of Raldh1-INH in HCC and establish the scientific premise for the development of isozyme-specific RALDH inhibitors as a new strategy in cancer immunotherapy.

[1]Department of Pathology and Laboratory Medicine, Perelman School of Medicine, University of Pennsylvania, Philadelphia, Pennsylvania. [2]BeiGene (Shanghai) Research & Development Co., Ltd., Shanghai, China. [3]National Center for Advancing Translational Sciences, National Institutes of Health, Rockville, Maryland. [4]Abramson Family Cancer Research Institute, Perelman School of Medicine, University of Pennsylvania, Philadelphia, Pennsylvania. [5]Department of Cell and Developmental Biology, Perelman School of Medicine, University of Pennsylvania, Philadelphia, Pennsylvania. [6]Institute for Immunology, Perelman School of Medicine, University of Pennsylvania, Philadelphia, Pennsylvania.

P. Yu and S. Cao contributed equally as coauthors of this article.

Corresponding Author: Malay Haldar, University of Pennsylvania, Philadelphia, PA 19104-6160. E-mail: mhaldar@pennmedicine.upenn.edu

Materials and Methods

Reagents

Key reagents are listed in Supplementary Table S1.

Animals

The University of Pennsylvania Institutional Animal Care and Use Committee (IACUC) approved all mouse experiments performed at the University of Pennsylvania. Pharmacokinetics (PK) studies were performed at the NIH and Pharmacon. Animal experiments performed at the NIH were conducted in compliance with institutional (NIH) guidelines. Animal procedures performed at Pharmakon were carried out according to guidelines approved by the IACUC of Pharmaron following the guidance of the Association for Assessment and Accreditation of Laboratory Animal Care.

Wild-type (WT) C57BL/6 mice were purchased from The Jackson Laboratory (cat. no. 000664). Immuodeficient NU/J mice were purchased from The Jackson Laboratory (cat. no. 002019). dnRAR[flox] mice were a generous gift from Dr. Cantorna Margherita at Pennsylvania State University. LysM[Cre] mice were purchased from The Jackson Laboratory (cat. no. 004781).

Generation of RALDH1-KO mice

Aldh1A1 knockout mice were created through the University of Pennsylvania's CRISPR/Cas9 Mouse targeting core facility. Two CRISPR RNAs (sequences below) were designed that encompassed an approximately 36 kilobase region within the mouse Aldh1A1 gene (Gencode Gene: ENSMUSG00000053279.8. Position: mm10 chr19:20,492,715–20,643,465).

Aldh1a1_5p_crRNA: CTGAGTTGGACCCTATATGG
Aldh1a1_3p_crRNA: GAGAATGTGTTGGTGCCTCG

A mix of pure Cas9 mRNA and the guide RNAs were injected into single-cell zygotes of C57BL/6 background mice. Founders were identified by a PCR-based genotyping protocol (details below) designed to detect the gene deletion. Founders were then bred to WT C57BL/6 mice to "fix" the allele. Heterozygous pups were identified by the aforementioned PCR-based genotyping and bred to each other to generate RALDH1-KO mice. Additional qRT-PCR assays were performed (described in "RNA isolation and qPCR analysis for gene expression") to confirm absence of the *Aldh1a1* transcripts.

PCR primers for RALDH1-KO genotyping (sequence 5'–3')

WT_9753: CAA CCC TGA GCA AAT CCT CCA C
WT_ 9754: GAC AGA TTG AGA GCA GTG TTT ACC C
Aldh1a1-KO_F1: TGA TAT GTC CCA GGA AGA TGA A
Aldh1a1-KO_R2: GGA CCG AGC ACT TGC CTA

PCR conditions

5 minutes at 94°C. 35 cycles of: (i) 30 seconds at 94°C, (ii) 30 seconds at 58°C, and (iii) 30 seconds at 72°C. Final extension of 7 minutes at 72°C followed by storage at 4°C. 248 base pairs band in knockouts and 665 base pairs band in WT detected by conventional gel electrophoresis.

Tumor cells

The details of the cell lines and culture media are described below. Upon receipt, cell lines were first expanded (two passages), authenticated (described below), and then frozen into aliquots for storage. The frozen stocks were thawed and expanded (average three passages) before experiments and discarded upon completion of individual experiments. When needed, the frozen stocks were reexpanded (aver-age of two passages), authenticated, and stored as frozen aliquots of additional stock.

The Huh1 cell line was a generous gift from Dr. Junwei Shi at the University of Pennsylvania. The cells were obtained in 2022 and authenticated on the basis of their morphology and growth characteristics in cell culture as well as the histology of the tumors formed upon transplantation into mice.

Huh7, SNU449, SNU398, HEP3B, PLC, HEPA 1–6, HEP55, and AL458A were from Dr. Celeste Simon at the University of Pennsylvania, who is also a coauthor on this article. The cells were obtained in 2021 and authenticated on the basis of their morphology and growth characteristics in cell culture as well as the histology of the tumors formed upon transplantation into mice.

Fibrosarcoma cell lines were obtained from Dr. Robert Schreiber at Washington University (St Louis, MO), and use in our laboratory has been described in a previous publication (11).

Tumor cell lines were cultured in DMEM (Thermo Fisher Scientific, cat. no. 10567014) with 10% FBS (GeminiBio, cat. no. 100–500) 1% Pen/Strep (Thermo Fisher Scientific, cat. no. 15140122), and 2 mmol/L glutamine (Thermo Fisher Scientific, 25030081). All cells were confirmed to be negative for *Mycoplasma* contamination as assessed by the MycoAlert *Mycoplasma* Detection Kit (Lonza, cat. no. LT07).

Human samples

A pathologist identified human formalin-fixed, paraffin-embedded (FFPE) samples of normal liver, normal kidney, HCC, gastrointestinal stromal tumors (GIST), and colorectal cancer from patients (deidentified) who underwent surgical resection for diagnostic or therapeutic purposes. 56 archived tissue blocks were selected and deidentified before sectioning and IHC. Approval from the Institutional Review Board at the University of Pennsylvania (Protocol 851744) was obtained before initiating the IHC study. As de-identified archived tissue blocks were used, specific written consent from patients was not required.

Normal donor human monocytes and T cells were collected by the Human Immunology Core (HIC) at the University of Pennsylvania and purchased by our laboratory from HIC. Written informed consents were obtained from donors by the HIC.

Implantation of tumor cells, tumor growth measurements, and survival analyses

Cultured Huh7, Huh1, Hepa 1–6, Hep55, and fibrosarcoma (as indicated in figure legends) tumor cells were detached using 0.25% trypsin (Gibco, cat. no. 25200056), washed once with 1x PBS, and counted before implantation. A total of $3{\sim}6{*}10^6$ tumor cells were implanted subcutaneously into shaved flanks of recipient mice. Tumor dimensions were measured using a caliper starting at the day indicated in the accompanying figure legend and every two to 3 days thereafter; volume was calculated by using formula Length*Width^2/2. Tumor volumes of 2,000 mm^3, tumor length of 2 cm or tumor ulceration were used as endpoints for survival analyses.

Flow cytometry of tissue samples

Tissue samples (murine tumors of the type indicated in the corresponding figure legends) were harvested and single-cell suspensions were generated by digestion with collagenase B and Dnase I (both Sigma-Aldrich) for 45 minutes at 37°C and filtration through 70 μmol/L cell strainers. Red blood cells were lysed using RBC Lysis Buffer (BioLegend). Samples were incubated for 20 minutes on ice with anti-mouse CD16/32 Fc Block (BD Biosciences), and subsequently stained on ice with primary-fluorophore conjugated antibodies for

identification of cell populations by flow cytometry. Flow cytometry was performed on an LSRII Flow Cytometer (BD Biosciences) and analyzed using FlowJo software (Treestar, version 10.8.1). A list of the antibodies used can be found in Supplementary Table S1.

In vitro tumor cell proliferation assay

A total of $1^* 10^4 \sim 2^* 10^5$ of Huh7, Huh1, Hepa 1–6, and Hep55 (as indicated in figure legends) tumor cells were plated in triplicate in 48-well plates or 6-well plates. Viable cell numbers were counted every day for three to 4 days.

In vitro treatments

Cultures of tumor cells or primary monocyte-derived cells were treated with C86, C91, C99, BMS 493 (Tocris, 3509) or Win 18446 (Tocris, 4736) at a time and concentration indicated in corresponding figure legends.

AldeRed assay

The AldeRed assay (EMD Millipore) was performed according to the manufacturer's instructions to identify cells with ALDH activity. In brief, single-cell suspensions of Huh7, Huh1, SNU449, SNU398, HEP3B, PLC, Hepa 1–6, Hep55, and AL458A cultured cells or single-cell suspension generated from enzymatic digestion of tumors generated from transplantation of these cells in mice (as indicated in figure legends) were incubated with a fluorescent and nontoxic ALDH substrate (AldeRed 588-A); the fluorescent product accumulates in cells proportional to their ALDH activity. The amount of fluorescence produced is measured by flow cytometry. The ALDH inhibitor diethylaminobenzaldehyde (DEAB, provided with the AldeRed assay kit) was used as a negative control for background fluorescence assessment.

Cell sorting

GFP-expressing Huh7 or Hep55 cells from CRISPR Knockout experiments were isolated using the FACS Jazz cell sorter at the Children's Hospital of Philadelphia Flow Cytometry Core Laboratory. Cells were identified and isolated on the basis of the GFP positivity alone on the cell sorter.

LC/MS for all-trans RA

For measurement of all-trans RA (ATRA), cultured cells were detached using trypsin, centrifuged, and the cell pellets stored at $-80°C$. ATRA was extracted from the frozen cell pellets and quantified at the Children's Hospital of Philadelphia Metabolomics Core using LC/MS as described previously (11).

Isolation of mouse bone marrow monocytes

Monocytes were isolated from bone marrow (BM) of C57BL/6 mice using the Mouse BM Monocyte Isolation Kit (Miltenyi Biotec) according to the manufacturer's instructions. Purity of monocyte was assessed by flow cytometry using CD11b, Ly6C, and Ly6G.

Intratumoral monocyte transfer

Monocytes were isolated from mouse BM of C57BL/6 mice and counted. Subsequently, a total of $1^* 10^6$ monocytes were resuspended in 50 μL 1x PBS and injected directly into established tumors at day 12 after tumor-cell implantation. Tumors were harvested at specified time points and analyzed by flow cytometry. For human monocytes, a total of $1^* 10^6$ cells were injected intratumorally as described above. This method of intratumoral monocyte transfer is described in detail in our previous publication (14)

In vitro and ex vivo mouse and human monocyte differentiation assays

Mouse monocytes were isolated from BM as described above and then cultured in RPMI-1640 (Thermo Fisher Scientific, cat. no. 11875085) with 10% FBS (GeminiBio, cat. no. 100–500). GM-CSF (20 ng/mL, peprotech 315–03) and IL4 (20 ng/mL, peprotech 214–14) were added for DC differention, whereas M-CSF (20 ng/mL, peprotech 315–02) was added for macrophage differentiation. Human monocytes were cultured in RPMI-1640 (Thermo Fisher Scientific, cat. no. 11875085) with 10% FBS (GeminiBio, cat. no. 100–500). GM-CSF (50 ng/mL, peprotech 300–03) and IL4 (50 ng/mL, peprotech 200–04) were added to cultures for DC differentiation, whereas or M-CSF (50 ng/mL, peprotech 300–25) was added for macrophage differentiation. RA (200 nmol/L; Sigma-Aldrich), C86 (100 nmol/L) or tumor conditioned medium was added at specified time points for indicated differentiation assays. Cellular identity and function of differentiated monocytes was assessed by flow cytometry and quantitative PCR (qPCR).

Depletion of cells in vivo

To deplete T cells, 200 μg of mouse CD3-specific antibody (clone 17A2) was administered intraperitoneally starting 3 days before tumor implantation and repeated every 3 to 4 days until mouse sacrifice.

To deplete macrophages, 200 μL of clodronate liposome (CloLipo) or PBS-liposome (CtrlLipo; both Liposoma) was administered intraperitoneally starting 3 days before tumor implantation and repeated every 4 days until mouse sacrifice. Macrophage depletion efficacy in spleen and within tumors was confirmed by flow cytometry using the canonical macrophage marker F4/80.

Drug treatment in vivo

Compound-86, 97 and 99 powder was dissolved in 20% HPβCD saline (2-Hydroxypropyl)-β-cyclodextrin). Drug was administered intraperitoneally or p.o. starting when tumor volume reached 50 to 150 mm³ and repeated every day. These compounds were described in our previous publication and produced at NCATs using methods outlined in that article (13).

200 μg of PD1-specific monoclonal blocking antibody (clone RMP 1–14) was administered intraperitoneally starting when tumor volume reached 50 to 150 mm³ and repeated every 2 days.

PK and toxicological studies

The PK studies were done at NIH or a commercial CRO, Pharmaron, using their in-house standard protocol.

1. For C91, IV and PO, performed at NIH using CD-1 mice; formulation: 20% HPbCD in saline
2. For C86, IV and PO, performed at Pharmaron using CD-1 mice; formulation: 20% HPbCD in saline
3. For C99, IV and PO, performed at NIH using CD-1 mice; formulation: 20% HPbCD in saline
4. IP PK of C86 at 10 and 30 mpk, performed at NIH using C57BL/6J mice; formulation: 60% PEG400 in DI water
5. Chow PK of C86, performed at Pharmaron using CD-1 mice at 10, 30, and 60 mpk, which the dose concentration in chow is 0.05, 0.15, 0.3 mg/g, respectively, based on the calculation of 5 g food consumption/mouse/d.

PK studies at the NIH were performed by the DMPK group. Male CD1 or C57BL/6J mice between 6 and 8 weeks old and weighing approximately 20 to 30 g were dosed with compound 86, compound 91, and compound 99 at 2 mg/kg (IV), 10 mg/kg (PO), and 10 or

30 mg/kg (IP). The compounds were formulated using a 20% hydroxypropyl-beta-cyclodextrin (HPbCD) solution in saline, was made on the day of dosing or directly before dosing. Each treatment group consisted of three mice, and plasma were collected at 5, 15, 30 minutes, and 1, 2, 4, 8, 12, and 24 hours after dose for intravenous administration and at 15, 30 minutes, and 1, 2, 4, 8, 12, and 24 hours after dose for PO administration. Approximately 0.025 mL of blood was collected from the dorsal metatarsal vein at each time point. The collected blood samples were then transferred into plastic microcentrifuge tubes containing heparin sodium as an anticoagulant. Samples were then centrifuged at $4,000 \times g$ for 5 minutes at $4°C$ to obtain plasma. Plasma samples were then stored in polypropylene tubes, quickly frozen, and kept at $-75°C$ until analyzed by LC-MS/MS. The following PK parameters were measured: Terminal half-life (T1/2), concentration at immediately after injection (C0), maximum concentration (C_{max}), time to reach max concentration (T_{max}), Clearance (CL), Volume of distribution (V_d), AUClast, and bioavailability (% F). Animals were also monitored during the in-life phase by once daily cage side observations; any adverse clinical signs were noted as part of the PK report.

Serum toxicological assays were performed by IDEXX Bioanalytics (Standard Tox Panel 62794). Briefly, peripheral blood was collected in regular eppendorff tubes by tail snips following a protocol approved by our institutional IACUC. Serum was prepared by letting the blood coagulate and inspected to confirm absence of hemolysis. The serum samples were stored in $-80°C$ until shipment to IDEXX.

Hematological studies, including complete blood count, were performed at IDEXX Bioanalytics. Briefly, peripheral blood was collected in heparin coated microhematocrit capillary tubes (VWR, 15401–560) by tail snips following a protocol approved by our institutional IACUC and stored at 4 degrees overnight before shipment to IDEXX.

RNA isolation and qPCR analysis for gene expression

Total RNA from mouse tissue samples and *in vitro* cultured cells was isolated using GenElute Mammalian Total RNA Miniprep Kit (Sigma) following the manufacturer's protocol. Total RNA from human FFPE samples was isolated by using the Quick-RNA FFPE Miniprep Kit (Zymo Research) using the manufacturer's protocol. 1,000 ng of RNA was used for reverse transcription using High Capacity RNA to cDNA Kit (Life Technologies).The cDNA product was $10\times$ diluted. 2.5 μL of this cDNA was used for qPCR for each sample. Three or more replicates were used for each reaction. Target gene expression was normalized to appropriate housekeeping gene indicated in the legends of figures showing RT-qPCR data. Expression fold was calculated as 2^-(C_t target gene $-C_t$ housekeeping gene). Quantitative PCRs were run on a Viia 7 real-time PCR system (Thermo Fisher Scientific). The following target and housekeeping genes were measured using the commercially available TaqMan probes (Thermo Fisher Scientific):

Mouse *Hprt* (Mm03024075_m1), Mouse *Irf4* (Mm00516431_m1), Mouse *Zbtb46* (Mm00511327_m1), Mouse *Mafb* (Mm00627481_s1), Mouse *Aldh1a1* (Mm00657317_m1), Mouse *Aldh1a2* (Mm00501306_m1), Mouse *Aldh1a3* (Mm00474049_m1), Human *HPRT* (4333768F), Human *IRF4* (Hs01056533_m1), Human *ZBTB46* (Hs01008168_m1), Human *MAFB* (Hs00271378_s1), Human *ALDH1A1* (Hs00946916_m1), Human *ALDH1A2* (Hs00180254_m1), and Human *ALDH1A3* (Hs00167476_m1.

Western blotting

A total of 1×10^7 cells were harvested and washed with PBS three times before 50 μL RIPA Lysis Buffer (Thermo Fisher Scientific,

cat. no. 89901) containing proteinase inhibitor (Thermo Fisher Scientific, cat. no. 78442) was added to the cell pellets and thoroughly mixed. Cell lysates were kept on ice for 30 minutes and centrifuged at $14,000 \times g$ for 15 minutes. The supernatant was collected, and the protein concentration measured using the BCA Protein Assay kit (Thermo Fisher Scientific, 23227). Next, 30-μg cell lysate for each sample was mixed with loading buffer (Thermo Fisher Scientific, cat. no. NP0007) to make a final volume of 20 μL and incubated at $95°C$ for 5 minutes. Samples were loaded on a precast 4%–15% SDS polyacrylamide gel (cat. no. 4561084, BIO-RAD), and run at 120V (constant voltage) for 40 to 60 minutes until the dye reached the bottom of the gel. Samples were transferred from the gel to polyvinylidene difluoride (PVDF) membrane in Tris-Glycine transfer buffer at 100 V for 1.5 hour at constant current (not to exceed 0.4 A). PVDF membranes were taken out from the blotting cassette and rinsed with TBST (10 mmol/L Tris-HCl, pH 8.0, 150 mmol/L NaCl, 0.05% Tween 20) for 5 minutes at room temperature (RT) 3 times. Nonspecific binding on the membrane was blocked with freshly prepared 5% nonfat dried milk (Labscientific, cat. no. M0841) for 1 hour on a shaker at RT for 1 hour. Aldh1a1-specific rabbit polyclone primary antibody (Invitrogen, cat. no. PA5–32127) and GAPDH-specific (14C10) rabbit mAb (Cell Signaling Technology, cat. no. 2118S) were diluted with 5% BSA at the ratio of 1:1,000 and incubated with the PVDF membrane at $4°C$ overnight. The membranes were washed three times for 5 minutes each with TBST, and incubated with horseradish peroxidase–conjugated secondary antibody (Cell Signaling Technology, cat. no. 7074) for 1 hour at RT. The membranes were washed three times for 5 minutes each with TBST, and incubated with ECL substrate (PerkinElmer, cat. no. NEL104001EA) for 1 minute before imaging using the ChemiDoc imaging system (Bio-Rad).

Establishment of CRISPR-mediated gene deletion tumor cell lines

Non-viral delivery of Cas9-RNPs was previously described (15). In brief, crRNA and tracrRNA (both Integrated DNA Technologies) were mixed at equimolar concentrations and were annealed by heating at $95°C$ for 5 minutes followed directly by hybridization for 15 minutes at RT. The annealed crRNA/XT-tracrRNA duplexes were mixed with Cas9 at a 3:1 molar ratio and were complexed by incubation at RT for ≥20 minutes. Nucleofection of Cas9-RNPs along with a GFP-expressing plasmid vector (supplied as part of the kit and used to identify cells undergoing successful nucleofection) was performed using Nucleofector 2 (Lonza). For the Huh7-RALDH1 knockout cell line, GFP-positive cells were sorted by FACS Jazz and loss of RALDH1 expression was confirmed by western blot. For the Hep55-RALDH1 knockout cell line, the GFP$^+$ cells were sorted by FACS Jazz and single-cell clones were established from sorted cells. Loss of ALDH1A1 was confirmed in individual clones with Sanger sequencing performed at the University of Pennsylvania core facility and western blots performed in-house.

Computational analyses of RNA sequencing data of human tumors

To compare *RALDH* isozyme expressions in HCCs versus other human tumors in the The Cancer Genome Atlas (TCGA) dataset, we used the cBioPortal website interface for gene expression query. To examine *RALDH* isozyme expression between different HCC molecular subtypes, we downloaded raw sequence counts for 371 primary tumor samples in The Cancer Genome Atlas (TCGA)-LIHC from the *Genomic Data Commons Data Portal*, and filtered them, retaining the

183 samples that were included in iClusters 1–3 as described in a previous publication (16). On a local workstation, several Bioconductor packages in R were used for subsequent steps. The count data were annotated with *biomaRt*. Principal component analysis (PCA) and plots were generated with *PCAtools*. Normalizations and statistical analyses were done with *DESeq2*. Exploratory GSEA pathway analysis was done with *fgsea* against the hallmark pathway set from the Molecular Signatures Database (MsigDB), using the *DESeq2* statistic as a ranking metric. Clustering was performed with the *degPatterns* function from the *DEGreport* package.

To examine the expression of *RALDH* isozymes in single-cell RNA sequencing (scRNA-seq) data of human HCC, we used a previously published and publicly available dataset (17). The authors created an atlas of this published scRNA-seq that can be queried using their webportal—http://omic.tech/scrna-hcc. ALDH1A1, ALDH1A2, and ALDH1A3 were used as gene query terms using all samples in the dataset for the scatter plot output.

Homology modeling

To build a homology model we used MOE (Molecular Operating Environment) software with default setting. The software MOE is a suite of different software tools developed by Chemical Computing Group Inc. The homology modeling algorithm within MOE comprises of the following steps. First, Initial Partial Geometry Specification: An initial partial geometry for each target sequence is copied from regions of one or more template chains. Where residue identity is conserved between the target sequence and its template, all heavy-atom coordinates are copied; otherwise, only backbone coordinates are copied. Second, Insertions and Deletions for correction of no assigned backbone coordinates. They are modeled from fragments of high-resolution chains from the Protein Data Bank that superpose well onto anchor residues on either side of the insertion area. Third, Loop Selection and Sidechain Packing: After the indel data collection is complete, a set of independent models is created. Loops are modeled first, in random order. For each loop, a contact energy function analyzes the list of candidates collected in the segment searching stage, taking into account all atoms already modeled and any atoms specified by the user as belonging to the model environment (e.g., a ligand bound to the template, or structural waters). These energies are then used to make a Boltzmann-weighted choice from the candidates, the coordinates of which are then copied to the model. Once all of the loops have been chosen, the side chains are modeled. Sidechain data are assembled from an extensive rotamer library generated by systematic clustering of conformations from rotamer library. A deterministic procedure based on Unary Quadratic Optimization is then run to select an optimal packing. After all of the backbone segment and side-chain conformations have been chosen for an intermediate model, hydrogens are added to complete valence requirements and the model is submitted to a series of minimizations designed to first relieve any serious steric strains, and then to prepare the model to be scored. It is then written to the output database, along with a number of quality assessment measurements that can flag any serious geometric problems. The fourth stage is Final Model Selection and Refinement. The final model is based on the best-scoring intermediate model. The final model is based on the best-scoring intermediate model. In this study, we used the electrostatic solvation energy, calculated used a Generalized Born/Volume Integral methodology. After the homology modeling procedure has finished, the final model was inspected using MOE's Protein Geometry stereochemical quality evaluation tools, including Ramachandran Maps.

IHC staining of mouse HCC tumor slides

Huh 7 xenograft tumor slides were dewaxed with citrisolv for 20 minutes, and 100%, 95%, 85%, 75% ethanol and ddH$_2$O for 3 minutes for each. Peroxidase was blocked with 3% H$_2$O$_2$ for 10 minutes at RT. Slides were then washed thrice with PBS and target retrieval for 15 min under high temperature. Slides were then blocked with Avidin/Biotin blocking kit (Vector laboratories) following the manufacturer's instructions. Rabbit anti-mouse CD163 (Abcam, Ab6720) was diluted 1:200 and incubated with the slides at 4°C overnight. Anti-rabbit secondary (Abcam) was diluted 1:200 and incubated with the slides at RT for 1 hour. The signal was amplified with the VECSTAIN ABC kit (Vector laboratories) and stained with the DAB substrate kit (Vector laboratories) following the manufacturer's instructions. The stained slides were scanned using a Leica Aperio Slide Scanner and analyzed with QuPath as described previously (18).

ALDH1A1 (D9Q8E) IHC on human tissue

Five-μm sections of FFPE tissue were stained using and antibody against ALDH1A1 (D9Q8E, Cell Signaling Technology 54135S, 1:400). Staining was done on a Leica Bond-IIITM instrument using the Bond Polymer Refine Detection System (Leica Microsystems DS9800). Heat-induced epitope retrieval was done for 20 minutes with ER1 solution (Leica Microsystems AR9961). All the experiment was done at RT. Slides were washed three times between each step with bond wash buffer or water. Slides were scanned on a Hamamatsu NannoZoomerS360.

Quantification and statistical analysis

Statistical significance was calculated between two groups by the Student unpaired *t* test. One-way ANOVA with the Tukey HSD after test was used to calculate statistical significance between multiple groups. Significance for survival was calculated by Kaplan–Meier with long-rank analysis. Analyses were performed using GraphPad Prism 8. Error bars represent SEM and a *P* value of <0.05 was considered statistically significant (*, $P < 0.05$; **, $P < 0.01$; ***, $P < 0.001$).

Data availability

The data generated in this study are available within the article and its Supplementary Data Files or upon request from the corresponding author.

Results

HCC expresses high levels of RALDH1 and RA

We previously identified an immune evasion pathway in sarcomas where tumor cell–derived RA promotes monocytes to differentiate into TAMs (11). To explore whether other types of cancer display similar RA-dependent immune evasion, we analyzed publicly available TCGA RNA-seq data from human tumors for expression of *RALDH* isozymes, finding high *RALDH1* transcripts in HCC (**Fig. 1A**). This was also confirmed through qRT-PCR in archived FFPE specimens from patients in our institution (Supplementary Fig. S1A). In contrast, the other two *RALDH* isozymes were not highly expressed in HCC when compared with other tumors in the TCGA RNA-seq database (Supplementary Fig. S1B and S1C). Next, we examined whether high *RALDH1* expression is associated with a specific subtype of HCC. A previous report described three distinct molecular subtypes of HCC based on DNA copy number, DNA methylation, mRNA expression, miRNA expression, and proteomics (16). Computational analyses of RNA-seq data downloaded from the aforementioned study (15) showed high *RALDH1*, but not *RALDH2* or *RALDH3*, in all subtypes, suggesting that *RALDH1* overexpression is a hallmark of HCC
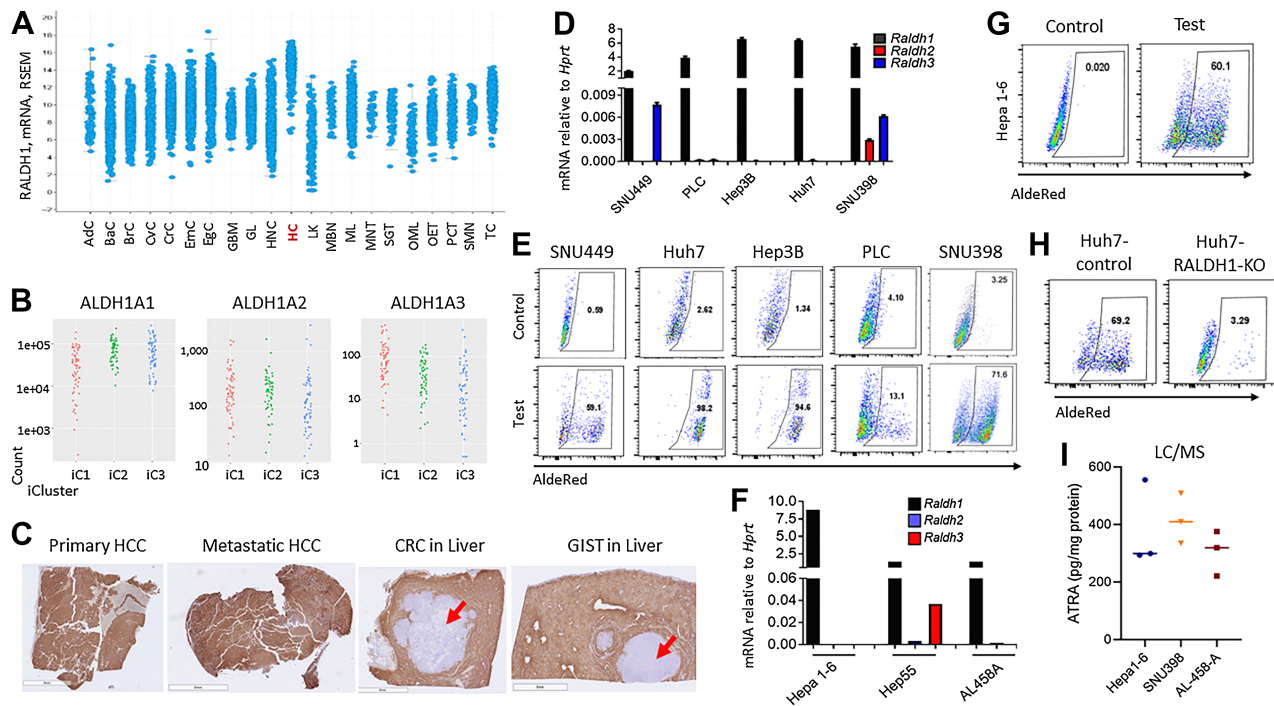
Figure 1.
HCCs overexpress RALDH1 to produce high levels of RA. **A,** Raldh1 mRNA levels (y-axis, RSEM, batch normalized) in different tumor types (x-axis) from TCGA data-based analyzed through the cBioPortal web interface. Data show higher expression of RALDH1 in liver cancer. AdC, adrenocortical carcinoma; BaC, bladder cancer; BrC, breast cancer; CvC, cervical cancer; CrC, colorectal cancer; EmC, endometrial cancer; EgC, esophagogastric cancer; GBM, glioblastoma; GL, glioma; HNC, head and neck cancer; HC, hepatobiliary cancer; LK, leukemia; MBN, mature B cell neoplasm; ML, melanoma; MNT. miscellenious neuroepithelial tumor; SGT, nonseminomatous germ cell tumor; OML, ocular melanoma; OET, ovarian epithelial tumor; PCT, pheochromocytoma; SMN, seminoma; TC, thyroid cancer. **B,** Raw sequencing counts for the 183 primary HCCs previously used to identify iCluster 1–3 molecular subtypes (16) were downloaded and the expression levels of the three Raldh isozymes calculated. Raldh1 levels are significantly higher than the other two isozymes in all three molecular subtypes. **C,** Human tumors (header) were stained with anti-RALDH1 antibody. Red arrows show tumor locations. Primary and metastatic HCC show strong RALDH1 staining whereas unrelated tumors, such as GIST and CRC show no staining. **D,** Transcript levels of Raldh1, Raldh2 and Raldh3 in multiple human HCC cell lines were measured by RT-qPCR. Raldh1 is the dominant isozyme expressed in all cell lines. **E,** AldeRed assay on human HCC cell lines. "Control" shows AldeRed fluorescence with aldehyde dehydrogenase inhibitor DEAB whereas "Test" shows the same without the inhibitor, which distinguishes fluorescence through RALDH activity from the background. The histograms are representative of ≥3 experiments. Numbers denote the percentage of cells within indicated gate. All HCC cell lines show high RALDH activity in all cells (Huh7 and Hep3B), majority of cells (SNU398 and SNU449), or some cells (PLC). **F,** Transcript levels of Raldh1, Raldh2 and Raldh3 in multiple murine HCC cell lines were measured by RT-qPCR. Raldh1 is the dominant isozyme expressed in all cell lines. **G,** AldeRed assay in murine HCC line Hepa1–6 showing high RALDH activity in the majority of cells. **H,** The Raldh1 gene was deleted from Huh7 cells by using CRISPR/CAS9 (RALDH1-KO cell line). Aldered assay performed on RALDH1-KO and the parental Huh7 cells show loss of Aldered positivity in the KO. **I,** LC-MS–based measurement of ATRA in the indicated murine and human HCC cell lines (x-axis).

(**Fig. 1B**). This was further confirmed by performing RALDH1 IHC on primary and metastatic HCCs, as well as unrelated tumors, which revealed strong RALDH1 staining in HCCs (**Fig. 1C**; Supplementary Fig. S1D).

The high level of expression of *RALDH1* in HCC tumors may come from tumor cells, immune infiltrates, or other stromal components. To identify the primary source, we examined a published and publicly available scRNA-seq of human HCC (17). Tumor cells and hepatocytes were the dominant producer of *RALDH1* in this dataset and expressed low amounts of *RALDH2* and *3* (Supplementary Fig. S1E). We next measured transcript levels of the three *RALDH* isozymes in five distinct human HCC cell lines, finding high *RALDH1* in all (**Fig. 1D**). To measure RALDH enzyme activity, we used the AldeRed assay. Consistent with elevated *RALDH1* transcripts, we detected AldeRed positivity in all human HCC cell lines tested (**Fig. 1E**). Likewise, murine HCCs also displayed high *Raldh1* and AldeRed positivity (**Fig. 1F** and **1G**). Of note, we showed that normal liver expresses all three *Raldh* isozymes whereas murine HCCs appear to

loose/suppress *Raldh2* and *3* (Supplementary Fig. S1F). Thus, HCCs are likely dependent on RALDH1 for RA production. To confirm this, we deleted *RALDH1* in human HCC cells using CRISPR/Cas9 and found dramatic reductions in AldeRed activity (**Fig. 1H**). Finally, we confirmed high RA in HCC cells through LC-MS–based measurement of ATRA, which is the dominant biologically active isomer of RA formed through RALDH1-catalyzed oxidation of Retinaldehyde (**Fig. 1I**).

Taken together, results in this section demonstrate that HCCs produce high levels of RA *via* RALDH1.

RALDH1 inhibitors abrogate RA production in HCC cells

RA can drive autocrine or paracrine signaling by binding RAR/RXR transcription factor heterodimers to regulate gene expression (12). Thus, reducing RA production by inhibiting RALDH enzymes and/or blocking RA signaling through RAR/RXR has the potential to curtail the RA-mediated tumor immune evasion we previously described (11). However, RA is an important morphogen and signaling molecule,
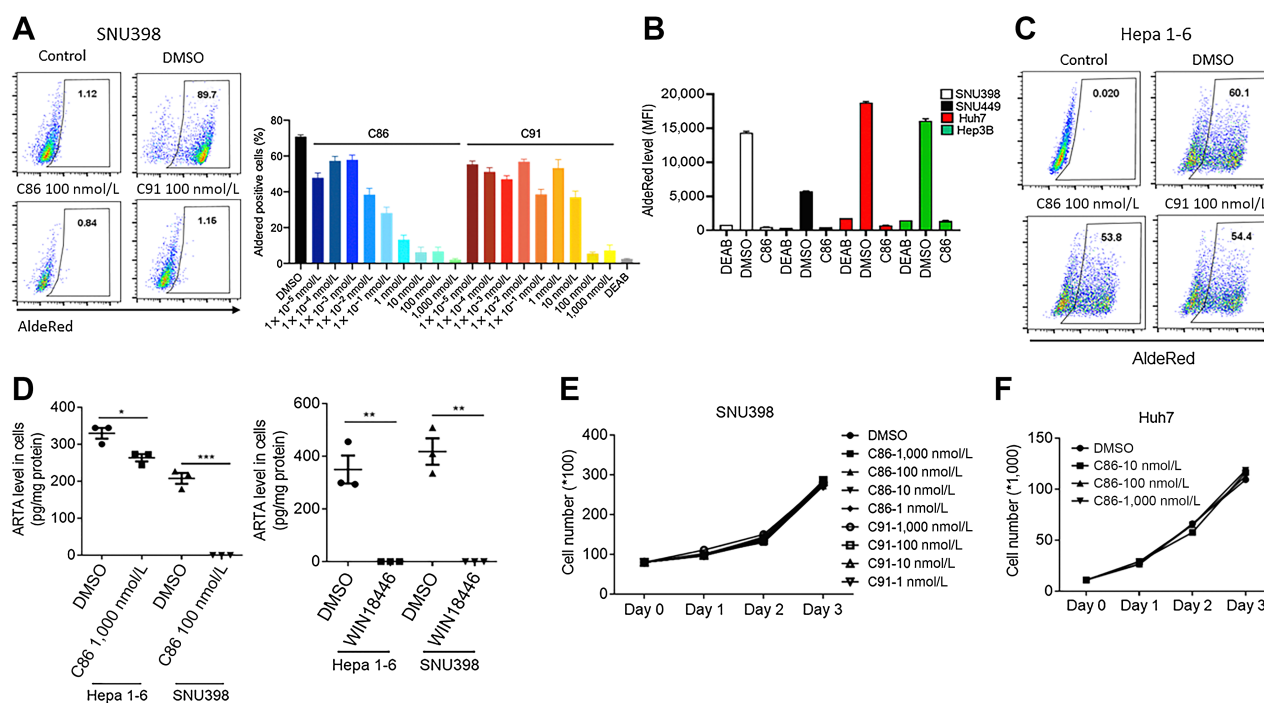
Figure 2.
Raldh1-INH show species-specific inhibition of RA production in HCC cells. **A,** SNU398 cells (human HCC cell line) were treated with the Raldh1-INH C86 or C91 for 24 hours. Representative two-color histograms on left shows loss of aldered fluorescence with Raldh1-INH whereas bar graph on right show quantitative changes in aldered-positive cells as a fraction of all cells when treated with different concentrations of the indicated Raldh1-INH. **B,** Median fluorescence intensity in aldered assay for different human HCC lines when treated with 100 nmol/L C86 for 24 hours. **C,** Representative two-color histograms show no change in aldeRed fluorescence when the murine HCC cell line (Hepa1–6) is treated with up to 1 µmol/L C86 or C91 for 24 hours. **D,** LC-MS for ATRA on Hepa1–6 (mouse HCC cell line) or SNU398 (human HCC cell line). Cells were treated with C86 (100 nmol/L for human or 1,000 nmol/L for mouse cells) or the nonspecific RALDH inhibitor WIN18446 (1,000 nmol/L) for 24 hours. WIN18446 inhibits both murine and human RALDH1 whereas C86 inhibition is specific to the human isozyme. Two independent experiments were performed with at least three replicates per experimental group. Unpaired t test, two-tailed. *, $P < 0.05$; **, $P < 0.01$; ***, $P < 0.001$. **E,** SNU398 cells were treated with different concentrations of C86 or C91 for 3 days. Cell proliferation was measured by counting live cell numbers at each time point. **F,** Huh7 cells were treated with different concentrations of C86 for 3 days. Cell proliferation was measured by counting live cell numbers at each time point.

which precludes global RA blockade as a therapeutic strategy. RAR and RXR have several isoforms that generate a diverse repertoire of RAR/RXR heterodimers. Although isoform-specific inhibitors of RARs and RXRs have been developed, they are used as tool compounds due to toxicity and lack of approved clinical indications. In contrast, RALDH isozyme–specific inhibitors as a strategy for RA blockade have not been adequately explored (19). We recently developed best-in-class RALDH1 inhibitors (Raldh1-INH) that showed good specificity and potency (13). Within this series, two inhibitors, Compounds 86 (C86) and 91 (C91), also known as NCT-505 and NCT-506, respectively, showed PK and pharmacodynamic (PD) profiles favorable to potential clinical applications (13). Thus, we examined whether C86 and/or C91 could inhibit RA production in HCC cells. Both inhibitors reduced AldeRed fluorescence in human HCCs, although C86 displayed higher potency (**Fig. 2A** and **B**; Supplementary Table S2). Thus, we primarily used C86 in subsequent experiments. C86 or C91 did not lead to compensatory increases in transcription of any other *RALDH* isozymes, which is consistent with the AldeRed data and demonstrates the efficacy of these inhibitors in suppressing RA production in HCC (Supplementary Fig. S2A). In contrast with human HCC, both inhibitors failed to reduce AldeRed fluorescence in murine HCC cells (**Fig. 2C**). LC/MS-based RA measurements confirmed the lack of RA suppression by C86 in murine HCC (**Fig. 2D**). Thus, C86 and C91 activity show species specificity. Homology modeling based on partial crystal structure of these Raldh1-INH suggests that differences in key drug-interacting amino acids between mouse and human may underlie this observation (Supplementary Fig. S2B). Finally, we confirmed that the reduced RA and AldeRed activity in human HCC cell lines with C86 or C91 was not due to increased cell death or reduced cell viability (**Fig. 2E** and **F**; Supplementary Fig. S2C).

Thus, results in this section demonstrate the efficacy of Raldh1-INH in abrogating RA production in human HCC cell lines.

HCC-derived RA regulates monocyte differentiation

To examine whether HCCs regulate monocyte differentiation, we cocultured primary human monocytes with either human HCC cell lines or cell culture supernatant (CM) from these cell lines. Flow cytometry analysis showed suppression of DC differentiation in the presence of HCC cells or CM (**Fig. 3A**). qRT-PCR analyses confirmed this, showing suppression of DC-associated genes and increased expression of macrophage-associated genes with CM (Supplementary Fig. S3A). These findings were reproduced in murine monocytes cultured with HCC cells or CM (**Fig. 3B**; Supplementary Fig. S3B). The effects were reversed when HCC cells were pretreated with the Raldh1-INH C86 (**Fig. 3A** and **B**; Supplementary Fig. S3A and S3B). Thus, HCC-derived RA regulates monocyte differentiation *in vitro*, which can be "rescued" by blocking RA production through Raldh1-INH.
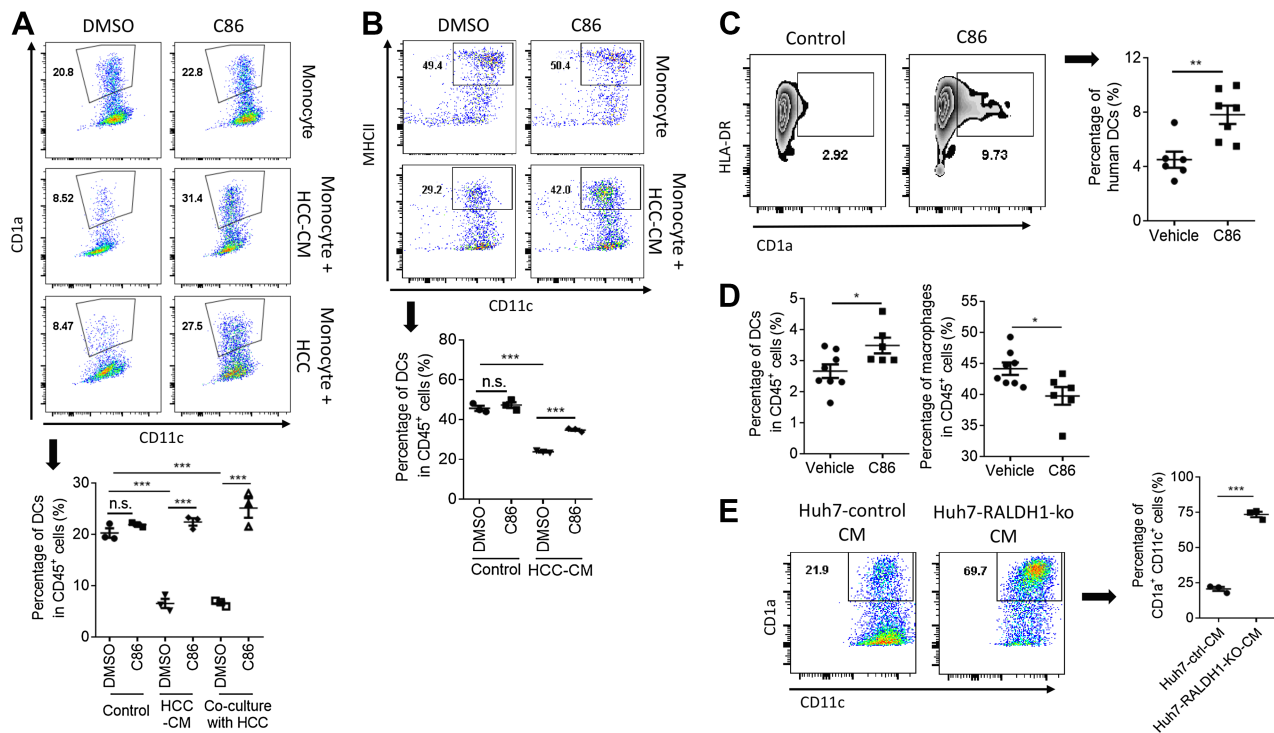
Figure 3.

RALDH1 inhibition blocks RA-mediated effects of HCC on monocyte differentiation. **A** and **B,** Circulating primary human monocytes from donors (**A**) or murine monocytes from bone marrow (**B**) were cocultured with SNU398 (Human HCC) cells or treated with SNU398-conditioned media (CM) in a DC differentiation system (GM-CSF and IL-4). Two-color histograms show the frequencies of DCs (CD11c$^+$CD1a$^+$ for human and CD11c$^+$MHCII$^+$ for mouse). The presence of SNU398 or its CM suppressed DC differentiation, which is reversed when SNU398 cells are treated with C86. Three or more independent experiments were performed with at least three replicates per experimental group. Unpaired *t* test, two-tailed. **C,** Huh7 (human HCC) cells were subcutaneously injected into flanks of NU/J mice. 12 days later the tumor size was about 50 mm^3 and C86 or vehicle treatment (10 mg/kg, i.p. daily injection) was started. On day 14, one million primary human monocytes (obtained from donors) were injected into these tumors. Five days after monocyte injection, mice were sacrificed and tumor tissue harvested for FCS analyses. Histogram shows DC (HLA-DR$^+$CD1a$^+$) differentiation of the injected human monocytes identified by human-specific CD45 (bar graph quantification on right). Three or more independent experiments were performed with at least three replicates per experimental group. Unpaired *t* test, two-tailed. **D,** Human monocytes were transplanted into Huh7 tumors similar to the strategy described in (**C**) and tumors were harvested 6 days after monocyte transplantation. Shown are the frequency of the host (murine) DCs (CD45$^+$F4/80$^-$CD11C$^+$MHCII-high) and macrophages (CD45$^+$F4/80$^+$) are quantified in a bar graph. Three or more independent experiments were performed with at least three replicates per experimental group. Unpaired *t* test, two-tailed. **E,** Circulating human primary monocytes from donors were cocultured with CM from Huh7-cells or the Huh7 cell line with Raldh1 deleted (RALDH1-KO) in a DC differentiation system (with GM-CSF and IL4). Shown are the representative FCM plot (histogram, left) and DC quantification (bar graph, right). Deletion of Raldh1 in tumor cells enhances DC differentiation from monocytes. Two independent experiments were performed with at least three replicates per experimental group. Unpaired *t* test, two-tailed. *, *P* < 0.05; **, *P* < 0.01; ***, *P* < 0.001; n.s., not significant.

Next, we tested this *in vivo* by transplanting immunodeficient (NU/J) mice with the human HCC cell line Huh7 and, once the tumors were established, performing intratumoral injection with primary human monocytes. Mice were treated with vehicle (control) or C86. In this setting, C86 selectively inhibited RALDH1 in the transplanted human cells (HCC and human monocytes) due to the species-specificity of this inhibitor described above. Five days after monocyte transplantation the tumors were analyzed by flow cytometry where human and murine leukocytes were distinguished using standard species-specific anti-CD45. Raldh1-INH treatment increased DC differentiation from transplanted human monocytes (**Fig. 3C**). This reflects the effect of reducing RA production in HCC cells and is consistent with results from the coculture experiments described above. Although a direct effect of the inhibitor on the transplanted human monocytes could also explain this observation, this is unlikely given that the host (murine) immune cells in the TME, which are insensitive to C86, also showed increased frequency of DCs and reduced frequency of macrophages (**Fig. 3D**). Furthermore, C86

treatment of monocytes *in vitro* did not alter their potential to differentiate into DCs (**Fig. 3A**). Finally, we confirmed RA as the key mediator of the aforementioned effects of HCCs on monocyte differentiation by using RALDH1-KO HCC cells, whereby CM from the knockout cells failed to suppress DC differentiation (**Fig. 3E**).

Taken together, data presented in this section show that Raldh1-INH suppresses HCC RA production and its attendant impact on monocyte differentiation.

## RA induces tumor-promoting attributes in monocyte-derived macrophages

Monocytes can differentiate into macrophages or DCs and we previously described the adaptive immune consequences of RA-mediated suppression of DC differentiation from monocytes in tumor immunity (11). However, whether and how tumors are affected by RA-induced macrophages remained unclear. We show above that HCC-derived RA can increase macrophage frequency in the TME (**Fig. 3D**). To examine whether RA also alters macrophage function, we adopted a

macrophage-tumor cotransplantation approach. Primary human monocytes were differentiated into macrophages in the presence or absence of RA, mixed 50:50 with the human HCC cell line (Huh7), and transplanted into immunodeficient NU/J mice. HCC cells transplanted without macrophages served as an additional control. RA-treated macrophages accelerated tumor growth compared with HCC cells transplanted alone or with control macrophages (**Fig. 4A**; Supplementary Fig. S4A). Therefore, we next assessed the overall impact of macrophages in HCC TME by depleting TAMs through intraperitoneal liposomal clodronate (CloLipo)—a common method to deplete macrophages (20). We confirmed TAM reductions with CloLipo and found reduced tumor growth in this setting (**Fig. 4B**; Supplementary

Fig. S4B). Thus, HCC-associated TAMs support tumor growth, a property that could be induced by high RA in the HCC TME.

To further explore this, we took the reductionist approach of coculturing RA-induced macrophages with HCC cells. First, we noticed that RA exposure increased macrophage numbers, which is consistent with our *in vivo* observations in the TME and suggests that RA may increase macrophage proliferation and/or survival (**Fig. 4C**). RA pretreated macrophages significantly increased tumor cell numbers compared with nontreated control macrophages; this effect was reversed when the macrophages were exposed to RAR signaling inhibitor BMS493 (**Fig. 4D**). Consistent with increased tumor cell numbers, CFSE labeling suggested increased tumor cell proliferation in
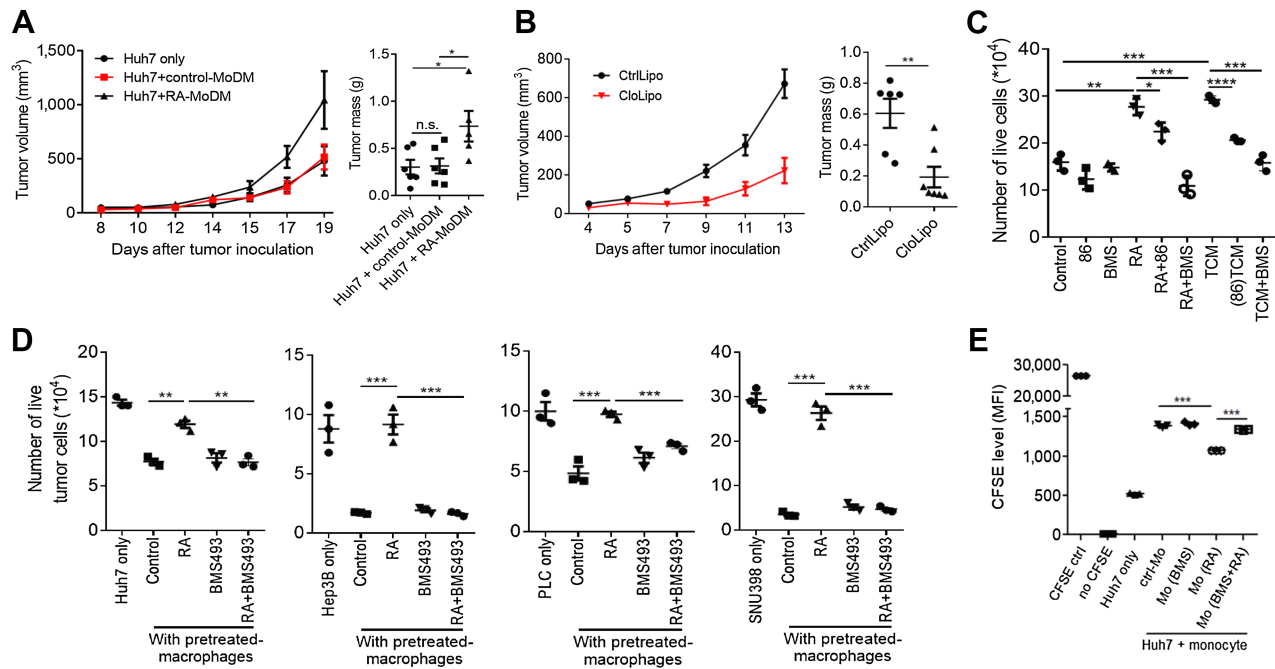
Figure 4.
Raldh1-INH blocks tumor supportive functions of monocytes and macrophages. **A,** Circulating primary human monocytes were collected from donors and cultured with MCSF (50 ng/mL) to generate macrophages. On day 3 of these cultures, DMSO or RA (100 nmol/L) was added to generate control monocyte-derived macrophages (Control-MoDM) or RA monocyte-derived macrophages (RA-MoDM), respectively. On day 7 of these cultures, macrophages were collected for each well after washing with 1XPBS, mixed with Huh7 cells at approximately 50:50 ratio, and the mix injected into the flanks of NU/J mice. Huh7 tumors cells that were not mixed with any macrophages before flank injection served as an additional control. Tumor volume was measured every 2 days (left graph). 19 days after tumor injection, mice were sacrificed and tumor weight (right graph) was measured. Tumor cells cotransplanted with RA-treated macrophages grew significantly faster than tumors cotransplanted with control macrophages or tumors transplanted without any macrophages. Three or more independent experiments were performed with at least three replicates per experimental group. Unpaired *t* test, two-tailed. **B,** Huh7 cells were subcutaneously injected to NU/J mice. When tumor size reached about 50 mm³, mice were intraperitoneally injected with liposomal clodronate (CloLipo; Liposoma, #C-015) and control liposomes (CtrlLipo; Liposoma, #P-015) at 200 μL/mice every 4 days. Tumor growth was monitored daily (left graph). 13 days after tumor cell transplantation, mice were sacrificed and tumor weight measured (right, bar graph). Macrophage depletion slowed tumor growth. Two independent experiments were performed with at least three replicates per experimental group. Unpaired *t* test, two-tailed. **C,** Macrophages were generated from primary human monocytes by culturing them for 7 days with M-CSF. Macrophages were then collected, washed, and seeded into new well with indicated compounds with or without tumor-conditioned media (CM; TCM). Three days later, cells were harvested, counted, and stained with PI for FCS analyses. Shown are the numbers of live macrophages (*y*-axis) under different experimental conditions (*x*-axis). RA and tumor-CM significantly increased macrophage numbers over other conditions, an effect that is reversed with reduced RA (C86 treated TCM) or RA signaling blockade (BMS493). Three or more independent experiments were performed with at least three replicates per experimental group. Unpaired *t* test, two-tailed. **D,** Different human HCC lines (*x*-axis, first legend of each graph) were cocultured for 3 days with macrophages pretreated with various compounds (*x*-axis). Cell proliferation was measured by counting live cell numbers (*y*-axis). RA treated macrophages increased tumor cell numbers compared with control macrophages, an effect that is reversed with RA signaling blockade (BMS493). Three or more independent experiments were performed with at least three replicates per experimental group. Unpaired *t* test, two-tailed. **E,** Primary human monocytes were differentiated into macrophages with M-CSF alone (control) or M-CSF with BMS493, RA, or RA + BMS493 (*x*-axis). After 7 days, macrophages differentiated under these conditions were harvested and cocultured with Huh7 human HCC cells (1:10 tumor cell: macrophage) that were labeled with carboxyfluorescein diacetate succinimidyl ester (CFSE). 72 hours later, the cells were washed, counted, and analyzed by FCS. HCC cell division is indicated by the extent of CFSE dilution (*y*-axis). Three or more independent experiments were performed with at least three replicates per experimental group. Unpaired *t* test, two-tailed. *, $P < 0.05$; **, $P < 0.01$; ***, $P < 0.001$; n.s., not significant.

the presence of RA-treated macrophages when compared with untreated control macrophages (**Fig. 4E**). These effects were recapitulated when HCC cells were grown with CM from RA-treated or control macrophages, suggesting that RA exposure may lead to production of a soluble "mitogenic" factor by macrophages (Supplementary Fig. S4C). Of note, tumor cells showed reduced proliferation when cultured with control (untreated) monocytes/macrophages, likely due to competition for nutrients (**Fig. 4D**). Pretreatment with RA abolished this suppressive effect, indicating the tumor-supportive effect of RA exposure. The experiment with CM (Supplementary Fig. S4C) clarified this further as the absence of monocytes/macrophages eliminated this competition for nutrients and "unmasked" the mitogenic effect of the soluble factor.

To summarize, results described in this section show that HCC-derived RA induces TAMs to produce factor/s that support HCC growth.

RALDH1 inhibitors suppress HCC growth

Data presented above show Raldh1-INH can alter monocyte differentiation and macrophage functions in the TME by blocking RA production in HCC cells. To examine the therapeutic implications, we transplanted huh1 and huh7 human HCC cell lines into immunodeficient mice and treated them with C86, finding significant tumor inhibition (**Fig. 5A**; Supplementary Fig. S5A). C86 treatment reduced RADLH activity, and hence RA production, in tumor cells but not infiltrating leukocytes (**Fig. 5B**). C86 displayed a dose–response, with tumor-suppressive effects at ≥10 mg/kg once daily dosing and weight loss observed only at higher doses of 40 mg/kg (**Fig. 5C** and **D**). Correspondingly, deletion of RALDH1 with CRISPR/Cas9 (RALDH1-KO) in HCC cells led to slower tumor growth *in vivo*, but not *in vitro* (**Fig. 5E**; Supplementary Fig. S5B). RALDH1-KO HCC tumors did not respond to C86 therapy, demonstrating that the tumor-suppressive effects of Raldh1-INH were primarily driven by on-target effects on RALDH1 (**Fig. 5E**). Next, we examined the role of TAMs in mediating the therapeutic effects of C86 by depleting them through CloLipo treatment. TAM depletion suppressed HCC growth and C86 treatment did not further suppress tumors in the absence of TAMs (**Fig. 5F**; Supplementary Fig. S5C). Thus, the therapeutic effects of reducing HCC-derived RA require the presence of TAMs.

Next, we tested whether HCC-derived RA acts directly on TAMs to promote tumor growth observed above. Toward this goal, we obtained mice that conditionally express a dominant-negative isoform of RAR from the Rosa26 locus (dnRARflox mouse; ref. 21). Expression of dnRAR leads to inhibition of RAR-mediated effects of RA. We crossed dnRARflox to Lysozyme 2-Cre mice (LysMCre), which express Cre recombinase in myeloid cells, including macrophages (22). Human HCC cells (Huh7) were transplanted after T-cell depletion into control and LysmCre: dnRARflox mice, revealing significant slowing of tumor growth and reduced TAMs with myeloid-specific dnRAR expression (**Fig. 5G**; Supplementary Fig. S5D and S5E). This suggests that tumor-derived RA induces tumor-promoting TAMs, which is consistent with data presented in previous sections. Nonetheless, dnRAR-mediated suppression of RA signaling is partial as it only inhibits RAR-mediated pathways and not the other RAR isoforms or RXRs and very high levels of RA can still overcome RAR-inhibition by dnRAR. To further examine the impact of blocking RAR signaling, especially in the context of therapy, we treated Huh7-bearing mice with the pan-RAR blocker BMS493 alone or in combination with Raldh1-INH. Although monotherapy with BMS493 or Raldh1-INH slowed tumor growth, the combination showed the greatest effect (**Fig. 5H**). Thus,

blocking RA production through Raldh1-INH and/or RA signaling through RAR inhibitors can suppress HCC growth.

### Reducing tumor-derived RA is the primary mechanism of tumor suppression by raldh1-INH

As described above, C86 and C91 show species specificity and do not inhibit murine RALDH1 (**Fig. 2C** and **D**). Thus, the aforementioned therapeutic effects on xenotransplantation-based tumor models represent a scenario where the drug can only work on transplanted tumor cells but not host cells and there are no T cells to mount antitumor immune responses. To overcome these limitations, we revisited our original published chemical series for Raldh1-INH and based on structure identified compound-99 (C99) as a potential inhibitor of murine RALDH1 (13). *In vitro*, C99 suppressed RALDH1 activity in both murine and human HCC cell lines (**Fig. 6A**), albeit at much higher (micromolar, **Fig. 6A**) concentrations compared with C86 (nanomolar range, **Fig. 2A**). Correspondingly, we found that the IC_{50} value of C99 to be significantly inferior to that of C86 (Supplementary Fig. S6A). Despite lower potency, C99 allowed us to overcome the aforementioned limitations of cross-species xenotransplantation models to further probe biological responses to Raldh1-INH.

C99 did not reduce proliferation or viability of the murine HCC cell line Hepa 1–6 *in vitro*, but it significantly suppressed tumor growth *in vivo* (**Fig. 6B** and **C**; Supplementary Fig. S6B and S6C). The human-specific C86 did not suppress murine Hepa 1–6 growth *in vivo* (**Fig. 6C**). C99 treatment, but not C86 treatment, reduced AldeRed activity in tumor cells and the frequency of TAMs within the TME (**Fig. 6D** and **E**). Furthermore, TAM depletion with CloLipo suppressed Hepa 1–6 tumor growth and rendered the tumors insensitive to C99 treatment (**Fig. 6F**). These findings mirror the effects of C86 on human HCC described in the previous sections and suggest that the tumor-suppressive activity of RALDH1 inhibitors is dependent on their ability to block RA production in tumor cells. To further confirm this, we tested C99 on the fibrosarcoma murine model of fibrosarcoma that expresses high levels of both *Raldh1* and *3* and is not solely dependent on RALDH1 for RA production; C99 did not suppress fibrosarcoma growth (**Fig. 6G**; Supplementary Fig. S6D).

Taken together, data in this section demonstrate the efficacy of Raldh1-INH in suppressing HCC growth through inhibition of RA production.

Raldh1-INH for HCC immunotherapy

As described above, C86 monotherapy showed therapeutic effects even in the absence of T cells in xenotransplant tumor models. C99 also suppressed tumor growth in syngeneic tumor models with intact adaptive immunity, but with two major limitations: C99 is much less potent compared with C86 or C91 and the murine Hepa 1–6 tumor cells tend to generate significant T-cell responses after subcutaneous transplantation in C57BL6/J mice, which occasionally leads to spontaneous delayed tumor rejection in our hands. These limitations make it difficult to examine the true therapeutic potential of C99 with Hepa 1–6. Nonetheless, it is important to examine the impact of full RALDH1 inhibition in the presence of T cells and test combinations with ICB. Toward this goal, we identified Hep55 as a murine HCC cell line that shows less spontaneous T-cell responses and no rejection in our hands. As shown in **Fig. 1F**, Hep55 cells also have high *Raldh1* expression. To overcome the limited efficacy of C99, we used a genetic approach and created RALDH1 deletion in Hep55 using CRISPR/-Cas9. Loss of *Raldh1* gene was compatible with normal growth of Hep55 cells *in vitro* but led to profound tumor suppression when the cells were transplanted *in vivo* (**Fig. 7A**; Supplementary Fig. S6E and
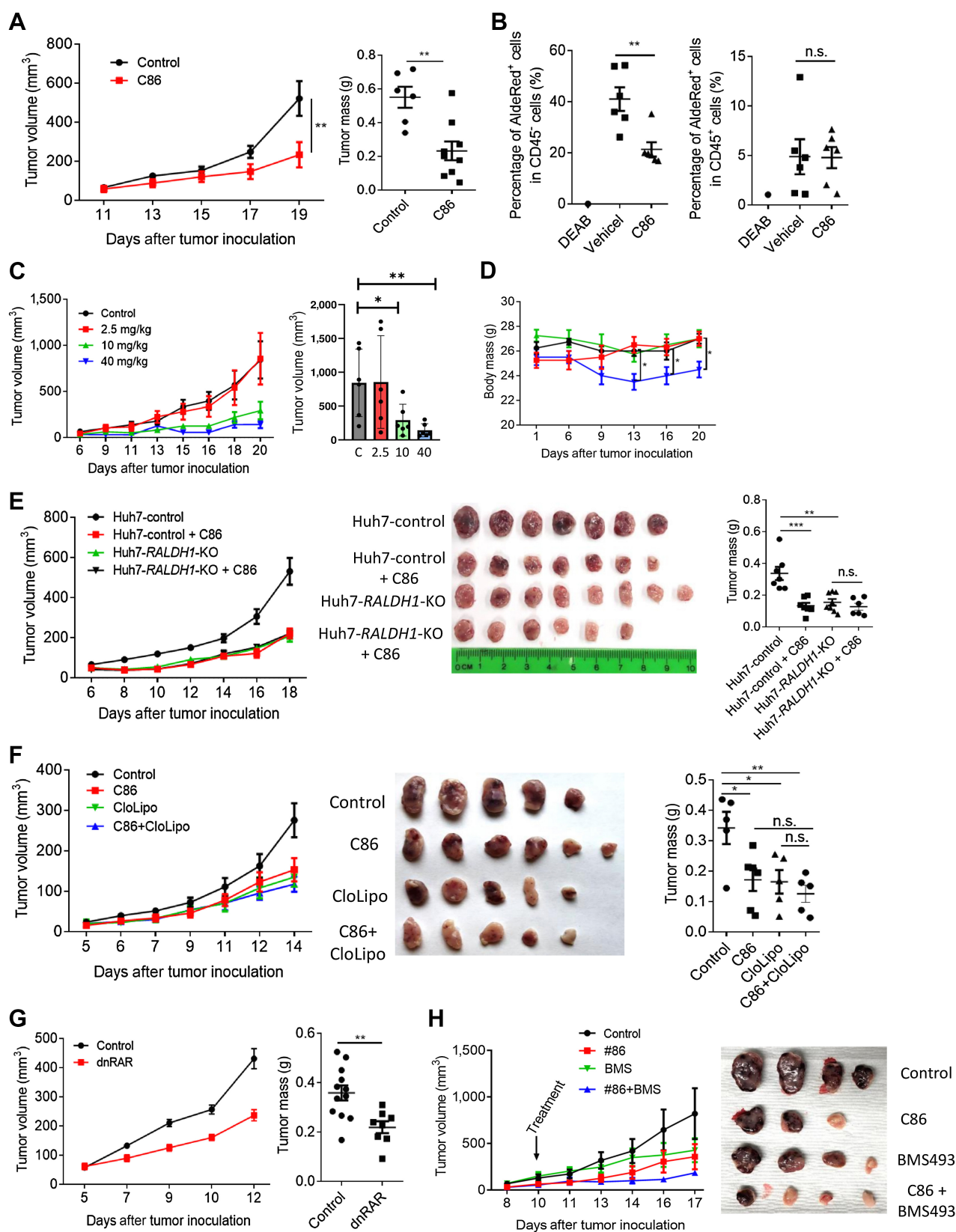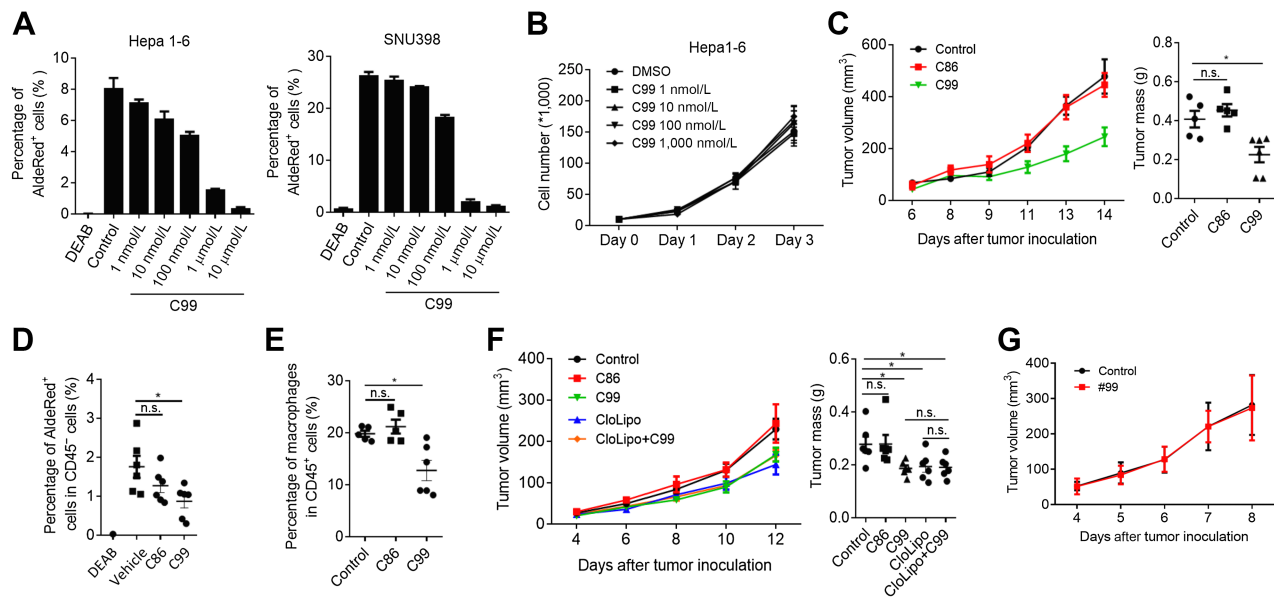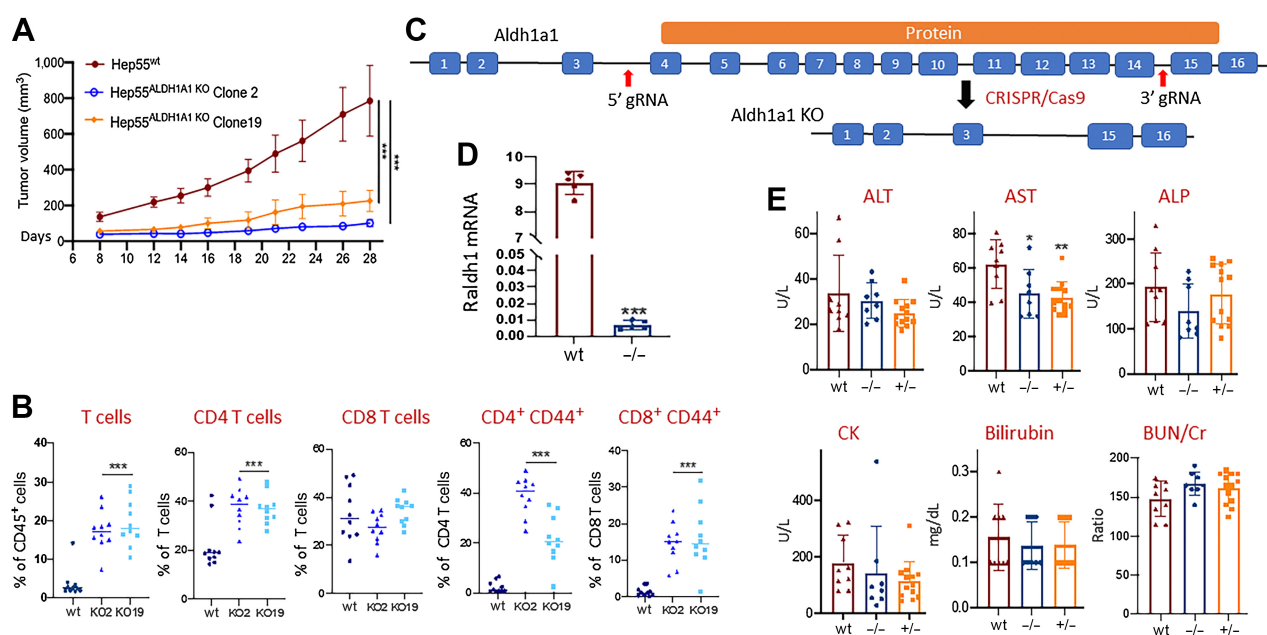
Figure 6.
C99 inhibits murine RALDH1 and suppresses murine HCC growth. **A,** AldeRed assay was performed on Hepa1–6 (murine HCC, left graph) and SNU398 (human HCC, right graph) cells with or without different concentration of C99 (x-axis). Shown is the percentage of Aldered-positive cells (y-axis) after 24 hours. Exposure to C99. Murine RALDH1 is sensitive to C99. **B,** Hepa1–6 cells were treated with different concentrations of C99 in vitro and the number of viable cells were counted at different time points. C99 does not reduce cell viability in vitro. **C,** C57BL6/J mice were implanted subcutaneously with Hepa1–6 cells and the tumor-bearing mice. To prevent spontaneous rejection of this cell line, mice were treated with anti-CD3. Once the tumors reached around 50 mm^3 size, mice were treated with C86 or C99 (i.p., 20 mg/kg) every day. Graph on the right shows tumor mass at end point. C99, but not C86, suppresses murine HCC growth. Two independent experiments were performed with at least three replicates per experimental group. Unpaired t test, two-tailed. **D,** Tumors in (**C**) were harvested at endpoint, single-cell suspension generated, and Aldered assay was performed along with surface staining with immune cell markers. Shown is the percentage of Aldered-positive cells in nonleukocytes (CD45 negative, mostly tumor cells) under the different treatment conditions. Two independent experiments were performed with at least three replicates per experimental group. Unpaired t test, two-tailed. **E,** FCS base frequency of Macrophages (F4/80$^+$ cells) within CD45$^+$ leukocytes in tumor tissues from experiment outlined in (**C** and **D**). Two independent experiments were performed with at least three replicates per experimental group. Unpaired t test, two-tailed. **F,** Hepa1–6 tumor-bearing NU/J mice were treated with chlodronate liposomes (CloLipo) and/or C86/C99. CloLipo treatment suppresses tumor growth and renders tumors insensitive to C99. Two independent experiments were performed with at least three replicates per experimental group. Unpaired t test, two-tailed. **G,** The murine fibrosarcoma (FS) cell line was implanted subcutaneously into C57BL6/J mice. Mice were treated with 25 mg/kg of C-99 or vehicle everyday starting one day after tumor cell transplantation. *, P < 0.05; **, P < 0.01; ***, P < 0.001; ns, not significant.

S6F). Tumor suppression was accompanied by significantly enhanced infiltration of RALDH1-KO tumors with activated T cells (**Fig. 7B**). Anti-PD1 treatment led to an even greater suppression of growth by RALDH1-KO Hep55 tumors (Supplementary Fig. S6G). Hep55 tumors showed infiltration with both pro- and anti-inflammatory

macrophages and the frequency of pro-inflammatory macrophages increased significantly with the loss of RALDH1 activity in tumor cells (Supplementary Fig. S6H and S6I). These findings are consistent with both macrophages and T cells driving the therapeutic effects of RALDH1 inhibition. In this context, it is worth noting that growth

---

Figure 5.
Raldh1-INH suppresses HCC growth by altering macrophage functions. **A,** Huh7 tumor-bearing NU/J mice were treated with C86 (i.p, 10 mg/kg) every day starting when tumor size was approximately 50 mm^3. Tumor volume was measured every 2 days. Bar graph on right shows tumor weight at endpoint. Three or more independent experiments were performed with at least three replicates per experimental group. Unpaired t test, two-tailed. **B,** AldeRed assay at endpoint on Huh7 tumor treated as described in (**A**). Graph shows percentage of Aldered-positive cells within CD45$^+$ leukocytes and CD45$^-$ cells (tumor + stromal cells). Data show selective inhibition of RA in mostly the tumor cells. Three or more independent experiments were performed with at least three replicates per experimental group. Unpaired t test, two-tailed. **C,** Huh7 tumor-bearing nude mice were treated with different dose of C86 every day. Tumor volume was measured every 2–3 days. Bar graph on right shows tumor volume at experimental endpoint. Two independent experiments were performed with at least three replicates per experimental group. Unpaired t test, two-tailed. **D,** Body weight measured every 3–5 days for the experiment outlined in **C** above. **E,** Parental Huh7 or RALDH1-KO Huh7 cells were implanted subcutaneously into NU/J mice and treated with C86 (i.p, 10 mg/kg) or vehicle (control) every day. RALDH1-KO tumors grew significantly slower than parental Huh7 and did not respond to C86 treatment. Bar graph on the right shows tumor weight at endpoint. Three or more independent experiments were performed with at least three replicates per experimental group. Unpaired t test, two-tailed. **F,** Huh7 tumor-bearing NU/J mice were treated with clodronate liposomes (CloLipo) and/or C86. CloLipo-treated tumors grew slower and did not respond to C86 treatment. Bar graph on the right shows tumor weight at endpoint. Two independent experiments were performed with at least three replicates per experimental group. Unpaired t test, two-tailed. **G,** Murine Hepa 1–6 tumors were implanted subcutaneously into C57BL6/J WT mice or LyM^{Cre}:Rosa^{dnRAR} mice. Expression of the dominant negative RAR in myeloid cells slows tumor growth. Two independent experiments were performed with at least three replicates per experimental group. Unpaired t test, two-tailed. **H,** Huh7 cells were implanted subcutaneously into NU/J mice. When tumor size reached about 50 mm^3, mice were intraperitoneally injected vehicle (control) or C86 daily with or without BMS493 treatment intratumorally every 3 days. BMS493 and C86 suppress tumor growth with the combination showing higher suppression than monotherapy. *, P < 0.05; **, P < 0.01; ***, P < 0.001; n.s., not significant.

Figure 7.
Pharmacokinetics of Raldh1-INH and synergy with immune checkpoint blockade. **A,** RALDH1 was deleted with CRISPR/Cas9 in the murine Hep55 HCC cell line. Two independent clones—2 and 19—were selected on the basis of the confirmation of gene deletion. Cell lines of indicated genotypes were implanted subcutaneously into immunocompetent syngeneic C57BL6/J mice and tumor size monitored over time. Tumor size at experimental endpoint is shown in Supplementary Fig. S6F. Three or more independent experiments were performed with at least three replicates per experimental group. One-way ANOVA. **B,** Tumors from (**A**) were harvested at endpoint (as shown in S6F) and T-cell infiltration analyzed by flow cytometry. Three or more independent experiments were performed with at least three replicates per experimental group. One-way ANOVA. **C,** Strategy for generating RALDH1-KO mice. Cas9 mRNA and the two guide RNAs (red arrows) were microinjected into single-cell zygotes. Founders were identified by a PCR screening protocol designed to detect the approximately 36kb deletion anticipated from dual cuts. The founders were then bred to C57BL/6 WT mice to "fix" the knockout allele. **D,** Confirmation of RALDH1 deletion in knockout mice through quantitative PCR performed with a murine RALDH1-specific TaqMan probe. Two independent experiments were performed with at least three replicates per experimental group. Unpaired t test, two-tailed. **E,** Serum from RALDH1-KO ($-/-$), heterozygous ($+/-$), and WT mice were used to perform serum toxicology analyses (standard tox panel no. 62794) through IDEXX bioanalytic services. Shown are a select few analytes from a larger panel. One experiment was performed with more than 5 replicates per genotype. One-way ANOVA. *, $P < 0.05$; **, $P < 0.01$; ***, $P < 0.001$.

of RALDH1-KO Hep55 tumors was suppressed to a greater extent than C86 treatment suppressed the growth of xenotransplanted human HCC. Although this could be due to a greater extent of RALDH1 inhibition with a genetic knockout, a more likely explanation is the presence of T cells in the syngeneic Hep55 model.

An important issue for the use of Raldh1-INH is on-target toxicity, especially given the expression of RALDH1 in normal liver. Although we have not observed any signs of toxicity with C86 and C91, a major caveat is the species specificity of these compounds. To examine the potential for on-target toxicity of RADH1 inhibition, we created genetic deletion of RALDH1 in mice (**Fig. 7C** and **D**). RALDH1-KO mice did not show any overt toxicity and developed normally compared with their WT siblings. Basic toxicological analyses of serum and complete blood count also did not reveal any abnormalities in RALDH1-KO and there were no significant weight differences between genotypes (**Fig. 7E**; Supplementary Fig. S7A and S7B). We also performed a standard panel of *in vitro* assays for off target effects (Eurofins Cereps Panlabs 85), which showed no concerns for off-target effects at the expected therapeutic concentration (Supplementary Table S3). Thus, the RALDH1-INH tested here are unlikely to cause serious toxicity.

Given the good efficacy and toxicity profile of RALDH1-INH, we next examined the PK and PD properties of the three RALDH1-inhibitors used in this study—C86, C91, and C99. We described above how C99 was less potent than C86 or C91. Here, we found that the half-

life of C99 was also significantly inferior to the other two Raldh1-INH (Supplementary Table S4). Although a better IC$_{50}$ value of C86 compared with C91 (Supplementary Table S2) was our rationale for using C86 in all our experiments, we found that the half-life of C86 was lower than that of C91 when the compounds were given through oral (PO) or intravenous routes (Supplementary Table S4). Nonetheless, we used intraperitoneal delivery in all *in vivo* experiments above, which is associated with superior PK profile compared with PO or intravenous route (Supplementary Tables S4 and S5). C86 also showed good biodistribution in various tissues when delivered intraperitoneally (Supplementary Table S5). Meanwhile, we formulated chow with C86 and examined PK/PD of the inhibitor over a 15-day period (Supplementary Fig. S7C). This approach showed good stability of C86 in chow and consistent drug exposure over time without affecting body weight (Supplementary Fig. S7C and S7D). Thus, Raldh1-INH show good efficacy and PK/PD profile for further preclinical development.

In summary, data presented here establish RALDH1 as a *bona fide* therapeutic target for HCC immunotherapy. We demonstrate its efficacy as monotherapy but given its unique mechanism of action, there are opportunities for combination with other treatment approaches. As a proof of concept, we demonstrated additive effects with ICB. Finally, we show that the basic PK/PD profile of Raldh1-INH are encouraging and support further development for eventual clinical trials. Besides illuminating a path forward for the treatment of HCC, a

common, lethal, and difficult to treat cancer, our work establishes RALDH inhibition as a viable therapeutic approach in other cancers.

Discussion

HCC is one of the leading causes of cancer-related death worldwide. Liver transplantation can be curative in the early stages of disease, but donor shortage leads to prolonged delays, by which time many cases progress beyond the eligibility criteria for transplantation. Therefore, even if Raldh1-INH monotherapy slows tumor progression without being fully curative, it could improve cure rates as a bridging therapy by allowing patients to successfully undergo transplantation. We also provide evidence that combination of ICB with Raldh1-INH may be more effective than either monotherapy, which warrants further investigation. Indeed, RALDH1-targeting is an entirely new approach of targeting antigen-presenting cells in the TME and could be combined with current systemic, surgical, and loco-regional therapies.

HCCs express high levels of *RALDH1* but lower levels of *RALDH3* and no detectable *RALDH2*, whereas normal liver expressed all three isozymes. Thus, HCCs are dependent on Raldh1 for RA production, which allows us to target RA production selectively in HCCs and limit on-target off tumor toxicity. Along these lines, it is reassuring to note that the RALDH1-KO mice showed no overt signs of toxicity. Nonetheless, the species specificity of RALDH1-INH poses some challenges for toxicological studies needed for human trials. Our homology modeling suggests that the inhibitor will likely work on primate *RALDH1*, which could be used as the animal model. Alternatively, we can introduce human *RALDH1* gene into the murine locus to generate a "humanized" murine model for such studies.

The present work builds upon our previous observation that tumor-derived RA blocks DC differentiation from monocytes, instead inducing monocytes to differentiate into TAMs (11). In that article, we mostly focused on the consequences of blocked DC differentiation, showing that RA blockade can rescue DC differentiation and induce T-cell responses. A notable observation in the present study is that RA blockade leads to significant tumor suppression even in the absence of T cells. We showed that this effect is mediated through macrophages and that CM from RA-exposed macrophages promoted HCC growth, suggesting that RA may induce production and release of a soluble mitogenic factor from macrophages. Transcriptional profiling of RA–exposed macrophages showed upregulation of several genes, such as Lipocalin2, that could potentially mediate this mitogenic effect, but further studies are needed (23). Although species specificity of our Raldh1-INH precluded us from directly addressing the role of T cells, it is very likely that the presence of T cells will augment the antitumor responses of the inhibitor based on enhanced T-cell infiltration and activation observed in RALDH1-KO tumors. Further support for this notion would be provided if there is clonal dominance of intratumoral T cells in RALDH1-KO tumors compared with parental tumors, and investigation of this is something we are currently pursuing. Nonetheless, this study highlights RA's impact on the TME beyond regulation of adaptive immune responses.

HCCs typically develop in the setting of chronic liver inflammation. With the advent of preventive and therapeutic strategies in viral hepatitis, the etiology of HCC is gradually shifting to nonviral inflammatory pathologies such as alcoholic steatohepatitis, nonalcoholic steatohepatitis, and nonalcoholic fatty liver disease. Whether RALDH1-mediated RA production plays a role in the development of HCC in these inflammatory settings is an important unknown. If true, Raldh1-INH could be even considered for preventative therapy.

Investigation of this could be conducted in inflammation-associated murine HCC models such as those induced by DEN. Indeed, the subcutaneous transplantation-based HCC models used in this study have some limitation and we plan to conduct additional studies with orthotopic transplants, patient-derived xenografts, and autochthonous HCC models to further explore the impact of Raldh1-INH. In closing, research presented in this article identifies RALDH1 as a new potential therapeutic target in HCC, reports development of new inhibitors of RALDH1, provides proof-of-concept for using RALDH1 inhibitors for HCC immunotherapy, and highlights a new approach to altering the tumor immune microenvironment.

Authors' Contributions

P. Yu: Conceptualization, formal analysis, investigation, methodology, writing–original draft, writing–review and editing. **S. Cao:** Conceptualization, formal analysis, investigation, methodology, writing–original draft, writing–review and editing. **S.-M. Yang:** Investigation, methodology. **G. Rai:** Conceptualization, formal analysis, investigation, methodology, project administration, writing–review and editing. **N.J. Martinez:** Investigation. **A. Yasgar:** Investigation. **A.V. Zakharov:** Investigation, methodology. **A. Simeonov:** Investigation. **W.A. Molina Arocho:** Methodology. **G.P. Lobel:** Investigation. **H. Mohei:** Investigation, methodology. **A.L. Scott:** Methodology. **L. Zhai:** Methodology. **E.E. Furth:** Investigation, methodology. **M.C. Simon:** Investigation. **M. Haldar:** Conceptualization, resources, supervision, funding acquisition, investigation, methodology, writing–original draft, project administration.

Note

Supplementary data for this article are available at Cancer Immunology Research Online (http://cancerimmunolres.aacrjournals.org/).

References

1. Llovet JM, Kelley RK, Villanueva A, Singal AG, Pikarsky E, Roayaie S, et al. Hepatocellular carcinoma. Nat Rev Dis Primers 2021;7:6.
2. Sung H, Ferlay J, Siegel RL, Laversanne M, Soerjomataram I, Jemal A, et al. Global cancer statistics 2020: GLOBOCAN estimates of incidence and mortality worldwide for 36 cancers in 185 countries. CA Cancer J Clin 2021;71:209–49.
3. Vogel A, Meyer T, Sapisochin G, Salem R, Saborowski A. Hepatocellular carcinoma. Lancet 2022;400:1345–62.
4. Finn RS, Ryoo B-Y, Merle P, Kudo M, Bouattour M, Lim HY, et al. KEYNOTE-240 investigators, pembrolizumab as second-line therapy in patients with advanced hepatocellular carcinoma in KEYNOTE-240: a randomized, double-blind, phase III trial. J Clin Oncol 2020;38:193–202.
5. Goswami S, Anandhan S, Raychaudhuri D, Sharma P. Myeloid cell-targeted therapies for solid tumours. Nat Rev Immunol 2023;23:106–20.
6. Pathria P, Louis TL, Varner JA. Targeting tumor-associated macrophages in cancer. Trends Immunol 2019;40:310–27.
7. Wculek SK, Cueto FJ, Mujal AM, Melero I, Krummel MF, Sancho D. Dendritic cells in cancer immunology and immunotherapy. Nat Rev Immunol 2020;20: 7–24.
8. Anderson DA, Murphy KM, Briseño CG. Development, diversity, and function of dendritic cells in mouse and human. Cold Spring Harb Perspect Biol 2018;10: a028613.
9. Haldar M, Murphy KM. Origin, development, and homeostasis of tissue-resident macrophages. Immunol Rev 2014;262:25–35.
10. Patel AA, Ginhoux F, Yona S. Monocytes, macrophages, dendritic cells and neutrophils: an update on lifespan kinetics in health and disease. Immunology 2021;163:250–61.
11. Devalaraja S, To TKJ, Folkert IW, Natesan R, Alam MZ, Li M, et al. Tumor-derived retinoic acid regulates intratumoral monocyte differentiation to promote immune suppression. Cell 2020;180:1098–114.
12. Cunningham TJ, Duester G. Mechanisms of retinoic acid signalling and its roles in organ and limb development. Nat Rev Mol Cell Biol 2015;16:110–23.
13. Yang S-M, Martinez NJ, Yasgar A, Danchik C, Johansson C, Wang Y, et al. Discovery of orally bioavailable, quinoline-based aldehyde dehydrogenase 1A1 (ALDH1A1) inhibitors with potent cellular activity. J Med Chem 2018;61: 4883–903.
14. Devalaraja S, Haldar M. Intratumoral monocyte transfer to examine monocyte differentiation in the tumor microenvironment. STAR Protoc 2020;1:100188.
15. Freund EC, Lock JY, Oh J, Maculins T, Delamarre L, Bohlen CJ, et al. Efficient gene knockout in primary human and murine myeloid cells by non-viral delivery of CRISPR-Cas9. J Exp Med 2020;217:e20191692.
16. Cancer genome atlas research network, Electronic address, wheeler@bcm.edu, Cancer genome atlas research network. Comprehensive and integrative genomic characterization of hepatocellular carcinoma. Cell 2017;169:1327–41.
17. Lu Y, Yang A, Quan C, Pan Y, Zhang H, Li Y, et al. A single-cell atlas of the multicellular ecosystem of primary and metastatic hepatocellular carcinoma. Nat Commun 2022;13:4594.
18. Bankhead P, Loughrey MB, Fernández JA, Dombrowski Y, McArt DG, Dunne PD, et al. QuPath: open source software for digital pathology image analysis. Sci Rep 2017;7:16878.
19. Harper AR, Le AT, Mather T, Burgett A, Berry W, Summers JA. Design, synthesis, and *ex vivo* evaluation of a selective inhibitor for retinaldehyde dehydrogenase enzymes. Bioorg Med Chem 2018;26:5766–79.
20. Nguyen T, Du J, Li YC. A protocol for macrophage depletion and reconstitution in a mouse model of sepsis. STAR Protoc 2021;2:101004.
21. Rajaii F, Bitzer ZT, Xu Q, Sockanathan S. Expression of the dominant negative retinoid receptor, RAR403, alters telencephalic progenitor proliferation, survival, and cell fate specification. Dev Biol 2008;316:371–82.
22. Clausen BE, Burkhardt C, Reith W, Renkawitz R, Förster I. Conditional gene targeting in macrophages and granulocytes using LysMcre mice. Transgenic Res 1999;8:265–77.
23. Krizanac M, Mass Sanchez PB, Weiskirchen R, Asimakopoulos A. A scoping review on lipocalin-2 and its role in non-alcoholic steatohepatitis and hepatocellular carcinoma. Int J Mol Sci 2021;22:2865.